PNAS RESEARCH ARTICLE | APPLIED PHYSICAL SCIENCES

Interplay between quantum anomalous Hall effect and magnetic skyrmions

Yang Li[a,b], Shengnan Xu[b], Jianfeng Wang[c], Chong Wang[d], Baishun Yang[a], Haiqing Lin[a,e], Wenhui Duan[b,f,g], and Bing Huang[a,e,1]

Edited by Angel Rubio, Max Planck Institut fur Struktur und Dynamik der Materie, Hamburg, Germany; received December 20, 2021; accepted April 3, 2022

Quantum anomalous Hall effect (QAHE) and magnetic skyrmion (SK) represent two typical topological states in momentum (*K*) and real (*R*) spaces, respectively. However, little is known about the interplay between these two states. Here, we propose that the coexistence of QAHE and SK may generate a previously unknown SK state, named the *RK* joint topological skyrmion (*RK*-SK), which is characterized by the SK surrounded by nontrivial chiral boundary states (CBSs). Interestingly, beyond the traditional SK state that can solely be used via creation or annihilation, the number and chirality of CBS in *RK*-SK can be tunable under external fields as demonstrated in Janus monolayer (ML) $MnBi_2X_2Te_2$ (X = S, Se), creating additional degrees of freedom for SK-state manipulations. Moreover, it is also found that external fields can induce a continuous topology phase transition from *K*-space QAHE to *R*-space SK in ML $MnBi_2X_2Te_2$, providing an ideal platform to understand the cross-over phenomena of multiple-space topologies.

two-dimensional magnetism | magnetic skyrmion | quantum anomalous Hall insulator | multiple-space topological phase transition

Significance

Quantum anomalous Hall effect (QAHE) and magnetic skyrmion (SK), as two typical topological states in momentum (*K*) and real (*R*) spaces, attract much interest in condensed matter physics. However, the interplay between these two states remains to be explored. We propose that the interplay between QAHE and SK may generate an *RK* joint topological skyrmion (*RK*-SK), characterized by the SK surrounded by nontrivial chiral boundary states (CBSs). Furthermore, the emerging external field–tunable CBS in *RK*-SK could create additional degrees of freedom for SK manipulations, beyond the traditional SK. Meanwhile, external field can realize a rare topological phase transition between *K* and *R* spaces. Our work opens avenues for exploring unconventional quantum states and topological phase transitions in different spaces.

Bringing the mathematical concept of topology to condensed matter physics leads to fascinating concepts and exotic phenomena in both momentum (K) space and real (R) space. The quantum anomalous Hall effect (QAHE) characterized by the nonzero Chern number ($\mathcal{C}$) and quantized conductance is a convictive example of the nontrivial topology in K space (1–3). As demonstrated in Fig. 1*A*, the nontrivial band structure of a QAH insulator supports the chiral edge state for dissipationless carrier transport, and the QAHE has been observed in the Cr-doped $(Bi, Sb)_2Te_3$ (4, 5) and odd-layer $MnBi_2Te_4$ (6–11). On the other hand, the magnetic skyrmion (SK) fingerprinted by the nonzero integer swirling number ($\mathcal{S}$) is a representative of topological nontrivial spin texture but emerging in R space (12–16). As demonstrated in Fig. 1*C*, the chiral noncollinear magnetic structure can generate an effective emergent electromagnetic field (16, 17), leading to the topological Hall effect (THE) (18–20). The SKs or magnetic skyrmion lattices (SkXs) have been observed in inversion-asymmetric three-dimensional helimagnets (21–23) and two-dimensional (2D) thin films (24–29).

Although there are intensive parallel studies on the QAHE (1–3) (Fig. 1*A*) and SK (12–16) (Fig. 1*C*), little is known about the interplay between these two states. The QAHE can exist in a 2D magnetic insulator with a strong spin-orbital coupling (SOC) effect (2, 3), while the SK usually originates from a strong Dzyaloshinsky–Moriya (DM) exchange interaction (30, 31) in an inversion-asymmetric system (12–16). In principle, the realization of both QAHE and SK in one system is allowed, regardless of the big challenge to discover such an ideal platform. Several attempts have been made to explore the novel topological states of free electrons and Dirac electrons in the effective external fields induced by SkXs (32, 33) or to design the concurrence of QAHE and magnetic domain–induced THE in magnetic sandwich heterostructures (34, 35), but the understanding of the interplay between K-space QAHE and R-space SK is still in its infancy.

As demonstrated in Fig. 1*B*, we propose that when SK exists in a QAH insulator, the Chern numbers inside ($\mathcal{C}_{\text{inner}}$) and outside ($\mathcal{C}_{\text{outer}}$) of the SK region are different, which may generate a previously unknown SK state, named *RK* joint topological skyrmion (*RK*-SK). The *RK*-SK is characterized by the existence of topologically protected chiral boundary states (CBSs), in which the number of CBSs is determined by $N_{\text{CBS}} = \mathcal{C}_{\text{inner}} - \mathcal{C}_{\text{outer}}$. The positive (e.g., Fig. 1 *D*, *Right*, anticlockwise arrow) or negative (e.g., Fig. 1 *D*, *Right*, clockwise arrow) sign of N_{CBS} reflects the different chirality. Beyond the conventional SK that can mainly be used via creation (i.e., $|1\rangle$) or annihilation (i.e., $|0\rangle$) (Fig. 1 *D*, *Left*) (13–15), the emerging N_{CBS} in *RK*-SK, which may be tunable under external fields, could create additional degrees of freedom (e.g., $|N_{\text{CBS}}\rangle, |0\rangle$) for SK-state manipulations (Fig. 1 *D*, *Right*). Meanwhile, the realization of continuous topological phase transition from K-space QAHE to R-space SK (or SkX) (Fig. 1*C*) state in one system via external fields (Fig. 1) is highly desired for understanding the cross-over of topologies in multiple spaces.

Author contributions: Y.L., H.L., W.D., and B.H. designed research; Y.L. and S.X. performed research; Y.L. contributed new reagents/analytic tools; Y.L., S.X., J.W., C.W., B.Y., H.L., W.D., and B.H. analyzed data; and Y.L. and B.H. wrote the paper.

The authors declare no competing interest.

This article is a PNAS Direct Submission.

[1]To whom correspondence may be addressed. Email: bing.huang@csrc.ac.cn.

This article contains supporting information online at https://www.pnas.org/lookup/suppl/doi:10.1073/pnas.2122952119/-/DCSupplemental.

Published May 13, 2022.

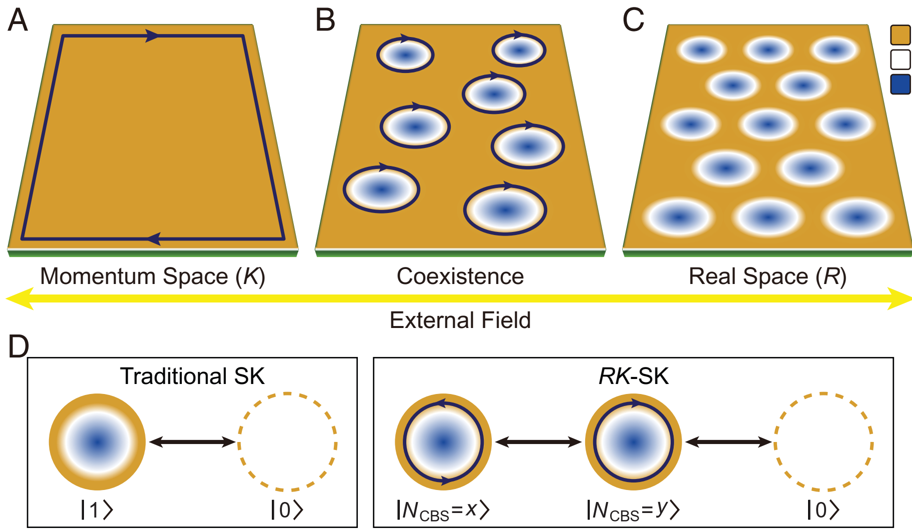

Fig. 1. Schematic diagram of the external field–tunable topological phase transition from K space to R space. (*A*) QAHE with chiral edge states. (*B*) *RK*-SK states with external field–tunable N_{CBS} may appear under certain conditions in the region where QAHE and SK can coexist. (*C*) An SkX state. (*D*) Comparison between traditional SK and *RK*-SK. *D*, *Left* shows that traditional SK can mainly be used via creation and annihilation. *D*, *Right* shows that there is an additional degree of freedom N_{CBS} in *RK*-SK (i.e., the number and chirality of N_{CBS}) for SK manipulation. Herein, x and y represent different values of N_{CBS}, in which the anticlockwise or clockwise arrows demonstrate the different chirality.

In this article, combining density functional theory (DFT) calculations and Monte Carlo (MC) simulations (*Materials and Methods*), we propose that applying both external biaxial strain (ε) and magnetic field (B_z) can realize a reversible topological phase transition between K-space QAHE and R-space SK/SkX states in monolayer (ML) $MnBi_2X_2Te_2$ (X = S, Se), in which our proposed RK-SK/SkX states with tunable N_{CBS} can appear in a certain region of the ε–B_z phase diagram. With the increase of ε, the K-space topology of ML $MnBi_2X_2Te_2$ will transform from high-$\mathcal{C}$ insulator ($\mathcal{C} = +2$) to low-$\mathcal{C}$ insulator ($\mathcal{C} = -1$) to trivial insulator ($\mathcal{C} = 0$) due to the ε-controlled different types of band inversions; simultaneously, the R-space topology can transform from trivial ferromagnetic (FM) phase to nontrivial SK phase to nontrivial SkX phase as the result of the dramatically different ε-dependent behaviors for collinear magnetic interaction and DM interaction. Therefore, the ML $MnBi_2X_2Te_2$ can serve as an ideal platform to understand the interplay and cross-over of multiple-space topological phenomena.

Results and Discussion

Band Topology of ML $MnBi_2X_2Te_2$. As shown in Fig. 2*A*, the ML $MnBi_2X_2Te_2$ is a Janus variant (36–39) created by replacing Te with X in the bottom two layers of ML $MnBi_2Te_4$ (40), forming an inversion-asymmetric structure. This septuple structure has the $P3m1$ symmetry, which contains three mirror operations and a threefold rotation with respect to the z axis (Fig. 2*B*). The Mn atoms locate at the center of the edge-sharing distorted octahedra, arranging in a triangle lattice and contributing to the long-range magnetic order. The same as the ML $MnBi_2Te_4$ (40), the FM configuration is the magnetic ground state of ML $MnBi_2X_2Te_2$ (*SI Appendix*, Fig. S1 and Table S1). The magnetic anisotropy energy (MAE) calculation shows that the easy axis of ML $MnBi_2X_2Te_2$ is along the z direction. The dynamical and thermodynamic stabilities of ML $MnBi_2X_2Te_2$ are confirmed by the phonon dispersion calculations (*SI Appendix*, Fig. S2) and ab initio molecular dynamics simulations (*SI Appendix*, Fig. S3),

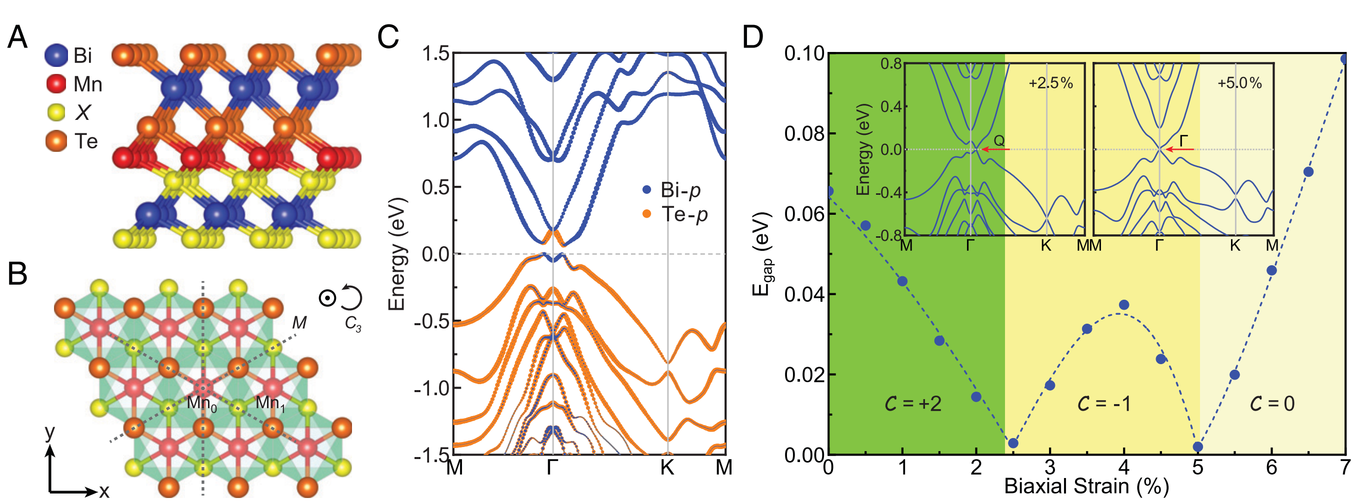

Fig. 2. Topological phase transition of ML $MnBi_2S_2Te_2$ in K space. (*A*) Side view of crystal structure of ML $MnBi_2X_2Te_2$. (*B*) Top view of the middle Te–Mn–X layer in ML $MnBi_2X_2Te_2$. (*C*) Orbital-projected band structure of ML $MnBi_2S_2Te_2$ in FM configuration with the SOC effect. Valence band maximum is set to zero. (*D*) Topological phase diagram of ML $MnBi_2S_2Te_2$ under tensible biaxial strain ε. *Insets* are the band structures near the two phase transition points.

respectively. It should be noted that Janus materials usually have higher energy compared with the disordered counterparts (*SI Appendix*, Figs. S4 and S5 and Tables S2 and S3). Given the successful growth of the Janus ML MoSSe and antisymmetrically decorated graphene (36–38), it is reasonable to expect that other Janus materials, including ML $MnBi_2X_2Te_2$, are also experimentally accessible. In the following, we will focus on the discussion of ML $MnBi_2S_2Te_2$ and only briefly mention the results of ML $MnBi_2Se_2Te_2$.

Fig. 2*C* shows the band structure of ML $MnBi_2S_2Te_2$ in the FM configuration. Similar to ML $MnBi_2Te_4$ (40), the electronic states around the Fermi level (E_F) are mainly contributed by Bi-$3p$ and Te-$3p$ orbitals; the Mn-$3d$ states that are extremely localized far away from E_F (*SI Appendix*, Fig. S6) exhibit much larger exchange splitting (∼7 eV) than crystal-field splitting (∼1 eV), leading to a high spin configuration of $d^5\uparrow d^0\downarrow$. Different from trivial insulator ML $MnBi_2Te_4$, the anticrossing between Bi–p_z and Te–$p_{x,y}$ states around the Γ-point at E_F in ML $MnBi_2S_2Te_2$ (*SI Appendix*, Fig. S7) can open a sizeable bandgap of ∼66 meV when the SOC effect is included, indicating a topological nontrivial nature. Indeed, the calculated Chern number is $\mathcal{C} = +2$, indicating that ML $MnBi_2S_2Te_2$ is an intrinsic high-$\mathcal{C}$ QAH insulator (41). Interestingly, although the band structures of ML $MnBi_2Se_2Te_2$ and ML $MnBi_2S_2Te_2$ are similar, the ML $MnBi_2Se_2Te_2$ is an intrinsic low-$\mathcal{C}$ QAH insulator ($\mathcal{C} = -1$) with a bandgap of ∼28 meV (*SI Appendix*, Figs. S6 and S8) (41).

Since the absolute volume deformation potentials of Bi–p_z and Te–$p_{x,y}$ orbitals are different, it is expected that the topological properties of ML $MnBi_2S_2Te_2$ in *K* space can be tuned by applying external biaxial strain ε. Interestingly, different from most known QAH insulators, it is found that multiple topological phase transitions can emerge under a reasonable ε-region. As shown in Fig. 2*D*, when $0.0\% < \varepsilon < 2.4\%$, the ML $MnBi_2S_2Te_2$ maintains the high-$\mathcal{C}$ insulator phase with $\mathcal{C} = +2$. When $\varepsilon = 2.4\%$, the first phase transition appears, induced by the band inversion at the Q point on the Γ–K line (Fig. 2 *D*, *Left Inset*). Due to threefold rotation symmetry, there are three equivalent Q points in the first Brillouin zone. Therefore, three band inversions happen at the same time, leading to the decrease of $\mathcal{C}$ by -3 (i.e., the ML $MnBi_2S_2Te_2$ is converted from a $\mathcal{C} = +2$ phase to a $\mathcal{C} = -1$ one). When $2.4\% < \varepsilon < 5.0\%$, the ML $MnBi_2S_2Te_2$ maintains the low-$\mathcal{C}$ insulator phase with $\mathcal{C} = -1$. When $\varepsilon = 5.0\%$, the second phase transition appears, induced by the band inversion at the Γ-point (Fig. 2 *D*, *Right Inset*). Consequently, the $\mathcal{C}$ further changes from -1 to 0 (i.e., ML $MnBi_2S_2Te_2$ is eventually converted to a trivial insulator phase) (more details are in *SI Appendix*, Fig. S9). Similarly, the diagram of the $+2 \rightarrow -1 \rightarrow 0$ topological phase transition is also found in ML $MnBi_2Se_2Te_2$ but in different ε-regions (*SI Appendix*, Figs. S10 and S11).

Spin Hamiltonian and Magnetic Interaction in ML $MnBi_2X_2Te_2$. The highly localized feature of Mn-$3d$ states (*SI Appendix*, Fig. S6) means that the magnetic property of ML $MnBi_2S_2Te_2$ can be captured using the spin Hamiltonian with the general form (42, 43)

$$H = \frac{1}{2}\sum_{i\neq j}\sum_{\alpha\beta}\mathcal{J}_{ij}^{\alpha\beta}S_i^\alpha S_j^\beta + \sum_i\sum_{\alpha\beta}\mathcal{A}_i^{\alpha\beta}S_i^\alpha S_i^\beta, \quad [1]$$

where S_i^α, S_j^β represent the spin operators; *i*, *j* are the magnetic sites; and α, β run over three cartesian indices. The first and second terms represent the exchange interaction and single-ion anisotropy (SIA), respectively, and the magnetic coupling matrix $\mathcal{J}$ and $\mathcal{A}$ can be obtained from the DFT calculations. Similar to ML $MnBi_2Te_4$ (40), the symmetric part of the nearest-neighbor (NN) exchange matrix of ML $MnBi_2S_2Te_2$ is diagonal with the isotropic exchange strength $J = (\mathcal{J}^{xx} + \mathcal{J}^{yy} + \mathcal{J}^{zz})/3$. The calculated $J = -2.27$ meV reflects an FM interaction, originating from the nearly ∼90° superexchange interaction (44, 45). Due to the symmetry of ML $MnBi_2S_2Te_2$, the SIA matrix $\mathcal{A}$ is diagonal with $\mathcal{A}^{xx} = \mathcal{A}^{yy}$, and the effective SIA parameter is $A = \mathcal{A}^{zz} - \mathcal{A}^{xx}$. The calculated $A = -0.17$ meV indicates that the z direction is the preferred spin orientation, consistent with the MAE calculations. Based on the isotropic exchange interaction and out-of-plane SIA, the Curie temperature (T_c) of ML $MnBi_2S_2Te_2$ is estimated to be ∼28 K (*SI Appendix*, Fig. S13). For ML $MnBi_2Se_2Te_2$, the smaller magnetic coupling strengths J and A lead to a lower T_c ∼23 K (*SI Appendix*, Figs. S12 and S13).

The antisymmetric part of the exchange matrix represents the DM interaction (30, 31), whose strength can be written as $D_\gamma = \varepsilon_{\alpha\beta\gamma}(\mathcal{J}^{\alpha\beta} - \mathcal{J}^{\beta\alpha})/2$, where $\varepsilon_{\alpha\beta\gamma}$ is the Levi–Civita symbol. The asymmetric structure leads to a nonzero DM interaction (46–51). For the ML $MnBi_2S_2Te_2$, the calculated NN DM vector $\mathbf{D}_{01} = (0.02, 0.52, -0.29)$ in units of millielectron volts of the Mn_0–Mn_1 pair (marked in Fig. 2*B*) lies in a plane perpendicular to the *x* axis (within a tiny numerical error), consistent with the restriction of the Moriya rule (31), due to a mirror plane passing through the middle point of the line between Mn_0 and Mn_1. Considering the C_{3v} symmetry, all six NN DM vectors of each Mn have a unified form $\mathbf{D}_{ij} = D_\parallel(\mathbf{e}_{ij} \times \mathbf{e}_\perp) + D_\perp\mathbf{e}_\perp$, where $\mathbf{e}_{ij}$ and $\mathbf{e}_\perp$ are the unit vectors along the Mn_i–Mn_j bond and *z* axis, respectively. Therefore, the six DM vectors surround each Mn in a staggered counterclockwise configuration (49–51). For ML $MnBi_2Se_2Te_2$, a relatively weaker DM interaction with $\mathbf{D}_{01} = (-0.02, 0.24, -0.16)$ in units of millielectron volts is obtained because the weaker electronegativity of Se than S causes weaker antisymmetric distortion in ML $MnBi_2Se_2Te_2$ than in ML $MnBi_2S_2Te_2$. Compared with the DM interaction in the surface of $MnBi_2Te_4$ (52), the intrinsic DM interactions in ML $MnBi_2X_2Te_2$ are sufficiently strong, which is the crucial ingredient for forming SK.

***RK*-SK State and Magnetic Phase Diagram in ML $MnBi_2X_2Te_2$.** Based on the above understanding, Eq. **1** can be simplified to

$$H = \frac{1}{2}\sum_{\langle i\neq j\rangle} J\mathbf{S}_i\cdot\mathbf{S}_j + \frac{1}{2}\sum_{\langle i\neq j\rangle}\mathbf{D}_{ij}\cdot(\mathbf{S}_i\times\mathbf{S}_j) + \sum_i AS_i^zS_i^z, \quad [2]$$

where $\langle i, j\rangle$ represents the summation runs over the NN sites *i*, *j*. As the DM interaction prefers to make the spin mutual perpendicularity, the interplay between the DM interaction and the collinear magnetic interaction may generate noncollinear magnetic structures (e.g., SK) (12–16). The competition between different magnetic interactions can be quantified using the factor $\alpha = 4\sqrt{JA}/\pi D$ (53, 54). The calculated $\alpha = 1.33$ in ML $MnBi_2S_2Te_2$ suggests the possibility for the existence of Néel-type SK in this system. Starting from Eq. **2**, we have performed the MC simulations to calculate the spin textures (55) in *R* space for ML $MnBi_2S_2Te_2$. As shown in Fig. 3*A*, the ground state of ML $MnBi_2S_2Te_2$ has a spin spiral (SS) configuration. To stabilize SK, the Zeeman term $H_z = g\mu_B S_z B_z$ should be included, where *g* is the Landé factor and μ_B is the Bohr magneton. As shown in Fig. 3*B*, due to the relatively strong DM interaction, the isolated SK with a radius $R_{SK} \sim 3.4$ nm appears under $B_z = 0.1$ T, with the swirling number $\mathcal{S} = -1$, and its spin direction continuously rotates from the $-z$ direction (in the center) to the *x*–*y* direction (in the boundary). Importantly, the nature of high-$\mathcal{C}$ phase in ML $MnBi_2S_2Te_2$ gives rise to the fundamentally different

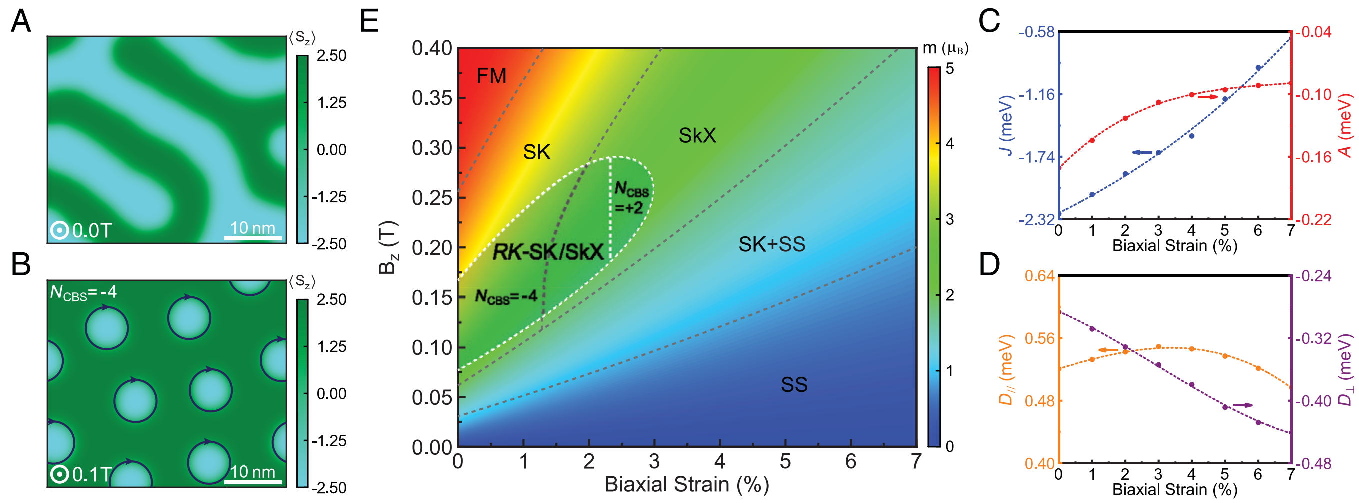

Fig. 3. Topological phase transition of ML $MnBi_2S_2Te_2$ in *R* space. Spin textures of ML $MnBi_2S_2Te_2$ under (*A*) $B_z = 0.0$ T and (*B*) $B_z = 0.1$ T. The color map corresponds to the spatial distribution of the out-of-plane spin component $\langle S_z \rangle$. (*C*) Isotropic exchange strength *J* and SIA parameter *A* of ML $MnBi_2S_2Te_2$ as a function of ε. (*D*) In-plane component $D_{\parallel}$ and out-of-plane component $D_{\perp}$ of the DM vector $\mathbf{D}_{01}$ for ML $MnBi_2S_2Te_2$ as a function of ε. (*E*) Magnetic phase diagram of ML $MnBi_2S_2Te_2$ as a function of ε and B_z. The gray-shaded area shows the regions where the *RK*-SK/SkX with ε-tunable N_{CBS} can appear.

$\mathcal{C}_{\text{inner}} = -2$ and $\mathcal{C}_{\text{outer}} = +2$ inside and outside the SK region, respectively, leading to the appearance of *RK*-SK with $N_{CBS} = \mathcal{C}_{\text{inner}} - \mathcal{C}_{\text{outer}} = -4$ (Fig. 3*B*). Since the estimated penetration depth ($\sim$3.6 nm) of CBS in ML $MnBi_2S_2Te_2$ (56) is comparable with the R_{SK} of SK, the *RK*-SK state can exist, although a tiny hybridization gap ($\sim$10 meV) may exist among these CBSs (*SI Appendix*, Fig. S16). Different from the ML $MnBi_2S_2Te_2$, the calculated $\alpha = 2.38$ in ML $MnBi_2Se_2Te_2$ gives rise to the absence of the SK state (*SI Appendix*, Figs. S10, S11, and S15).

The tunable magnetic interactions via strain may further modulate the topological spin textures of ML $MnBi_2S_2Te_2$. Generally, the increase of ε will increase the bond angle $\theta_{\text{Mn}-X-\text{Mn}}$, weakening the FM superexchange interaction (57), and increase the localization of Mn-3*d* states, weakening the *p*–*d* hybridization between Mn and its NN ligands. These result in the decrease of *J* with the increase of ε, as shown in Fig. 3*C*. A similar weakening behavior is found for *A*, originating from the weakening of *p*–*d* hybridization and crystal-field splitting. As shown in Fig. 3*D*, it is surprisingly found that in contrast to *J* and *A*, the in-plane *D* ($D_{\parallel}$) is insensitive to the variable ε, and the out-of-plane *D* ($D_{\perp}$) can even be largely increased when ε increases. Since the DM interaction derives from the SOC effect on the isotropic exchange interaction, its strength is determined by the exchange interaction of adjacent magnetic sites as well as the SOC-induced orbital coupling between the occupied and empty Mn-3d states (31, 58). Therefore, although the exchange interaction weakens as the ε increases, the reduced energy gap between occupied and empty states may enhance their interorbital coupling, resulting in the unexpected ε-dependent behaviors of the DM interaction in Fig. 3*D*. For ML $MnBi_2Se_2Te_2$, a similar ε-dependent magnetic interaction is observed (*SI Appendix*, Fig. S12).

The dramatically different ε-dependent J/A and D strongly indicate that the noncollinear magnetic structure will be rather sensitive to ε. Fig. 3*E* shows the magnetic phase diagram of ML $MnBi_2S_2Te_2$ as a function of ε and B_z. When $B_z = 0.0$ T, the ML $MnBi_2S_2Te_2$ maintains the SS phase, and the width of the worm-like pattern decreases as the ε increases (*SI Appendix*, Fig. S14). Under a moderate B_z (e.g., $B_z \sim 0.2$ T), the sparsely isolated SKs appear when $0.0\% < \varepsilon < 1.5\%$, as the relatively weak DM interaction leads to $\alpha > 1.0$. When $1.5\% < \varepsilon < 3.0\%$, $\alpha < 1.0$, the SKs with high density arrange in a lattice form (i.e., the SkX phase appears); when $\varepsilon > 3.0\%$, the contribution of DM interaction becomes more important, leading to the appearance of SS spin texture, and the system enters the phase of coexistence of SK and SS states. Since B_z tends to align spins in the *z* direction, the size of SK could be tunable by B_z (e.g., it will gradually decrease as the B_z increases) (*SI Appendix*, Fig. S14). Therefore, when $B_z > 0.2$ T and $0.0\% < \varepsilon < 1.5\%$, the system will eventually enter the FM phase. When $B_z > 0.2$ T and $\varepsilon > 1.5\%$, $\alpha < 1.0$, the B_z will eliminate the worm-like pattern and results in SkX phase.

External Field–Tunable *RK*-SK/SkX States and Topology Cross-Over from *K* Space to *R* Space. In general, the *RK*-SK state can appear in the coexistence phase of the QAH insulator and SK as long as the CBS with well-defined chirality surrounding the *RK*-SK can be well distinguished from the bulk states. Here, we focus on the *RK*-SK/SkX with tiny hybridization gap opening among their CBSs [i.e., their R_{SK} should be at least comparable with the penetration depth of CBS (59)], so that the original chirality of CBS could be largely maintained. As shown in the gray-shaded area of Fig. 3*E*, when $0.0\% < \varepsilon < 2.4\%$ and under an appropriate B_z, the ML $MnBi_2S_2Te_2$ maintains the $\mathcal{C} = +2$ phase, and $N_{CBS} = -4$ results in the *RK*-SK encircled by four CBS modes (Fig. 3*B*). When $\varepsilon > 2.4\%$, ML $MnBi_2S_2Te_2$ is converted to the $\mathcal{C} = -1$ phase; therefore, the N_{CBS} will be changed from -4 to $+2$ (i.e., the *RK*-SK is now encircled by two CBS modes with opposite chirality). Interestingly, as shown in Fig. 3*E*, while the $N_{CBS} = -4$ state can exist either in isolated *RK*-SK or in *RK*-SkX in the different regions of the ε–B_z phase diagram, the $N_{CBS} = +2$ state can solely exist in *RK*-SkX. Although the number and chirality of CBS in *RK*-SK can be tunable via external fields, the contribution of CBS to the global transport properties of the system may depend on the exact Fermi-level position (*SI Appendix*, section VIII, which includes ref. 60). It should be noted that these CBSs may be visible by the local *dI*/*dV* spectrum in experiments, providing an additional degree of freedom for information storage during local manipulation of individual SK. For ML $MnBi_2Se_2Te_2$, the *RK*-SK/SkX states cannot exist as the QAHE phase and SK states cannot coexist (*SI Appendix*, Figs. S10, S11, and S15).

Other than the *RK*-SK/SkX states, as shown from Fig. 3*E*, it is interesting to find that the multiple-space topology cross-over

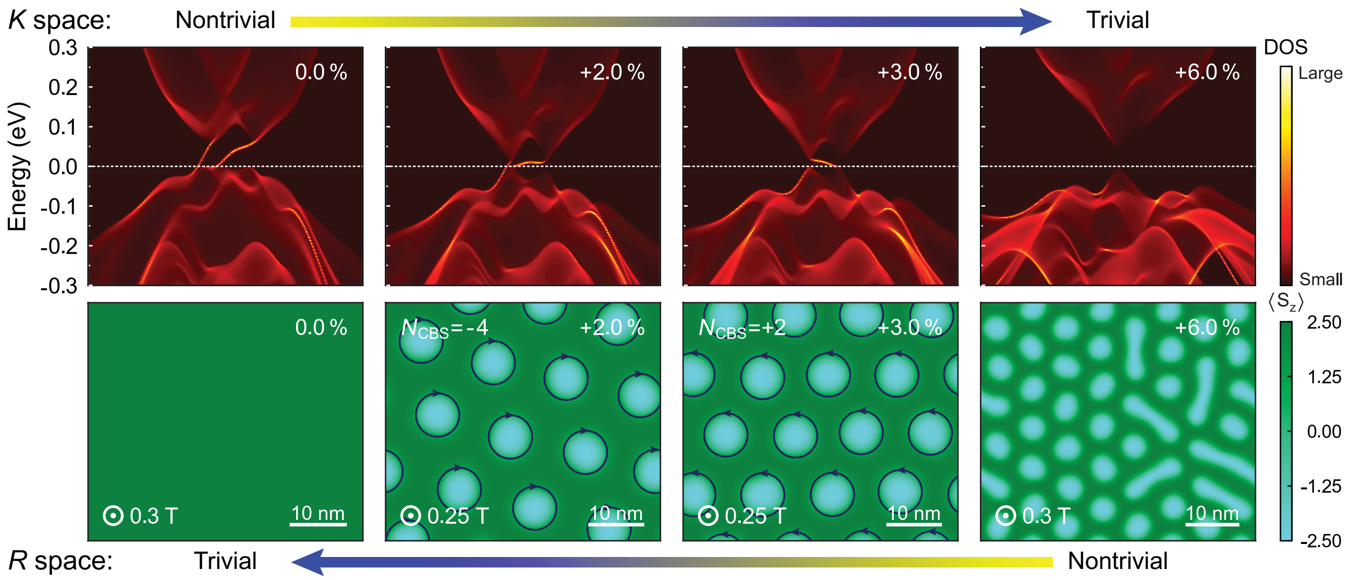

Fig. 4. External field–tunable multiple-space topology cross-over from K space to R space in ML $MnBi_2S_2Te_2$. Evolution of edge states in K space (*Upper*) and spin textures in R space (*Lower*) with the increase of ε. The intensity of density of states (DOS) for edge states are also marked in the figure.

can be achieved in ML $MnBi_2S_2Te_2$ via tuning external fields. For example, as shown in Fig. 4, we choose four different ε-cases to calculate their K-space edge states and R-space spin textures. In K space, when $\varepsilon = 0.0\%$ and $\varepsilon = 2.0\%$, the two "in-gap" chiral states with ε-tunable positive group velocity clearly show the topological nontrivial nature of ML $MnBi_2S_2Te_2$ in $\mathcal{C} = +2$ phase. When $\varepsilon = 3.0\%$, the number and group velocity of "in-gap" chiral states are changed to one and negative value, respectively, consistent with $\mathcal{C} = -1$ phase of ML $MnBi_2S_2Te_2$ in this ε region; when $\varepsilon = 6.0\%$, the vanishing chiral edge state represents a topological trivial state of ML $MnBi_2S_2Te_2$. On the other hand, in R space, when $\varepsilon = 0.0\%$, the ML $MnBi_2S_2Te_2$ exhibits the trivial FM configuration. When $\varepsilon = 2.0\%$, the Néel-type RK-SkX appears with $N_{CBS} = -4$. When $\varepsilon = 3.0\%$, the Néel-type RK-SkX with $N_{CBS} = +2$ appears. When $\varepsilon = 6.0\%$, the system transforms into the mixing phase with the coexistence of smaller-sized SKs and worm-like pattern SS as the result of stronger DM interaction. Therefore, other than the RK-SK states with tunable N_{CBS}, an ideal topology cross-over in multiple spaces, as proposed in Fig. 1, can also be well achieved in ML $MnBi_2S_2Te_2$. For ML $MnBi_2Se_2Te_2$, a similar multiple-space topology cross-over is also found but without the appearance of RK-SK states (*SI Appendix*, Figs. S10, S11, and S15).

Finally, it should be noted that the ML $MnBi_2Te_4$ has been successfully synthesized in the experiments (9, 61). On the other hand, the approaches for growing 2D Janus structures have also been successfully demonstrated in several different materials, creating many exotic applications (36–38). Therefore, we expect that the Janus ML $MnBi_2X_2Te_2$ system associated with the quantum phenomena we proposed here could stimulate the experimental efforts in the future.

Outlook and Conclusion

To further control the skyrmion size, as the ML $MnBi_2X_2Te_2$ has out-of-plane polarization, we expect that the fine tuning of magnetic interactions may be achieved via the external electric field apart from external strain, leading to the effective manipulation of skyrmion size. In addition, despite the similar CBS that may exist in the domain walls between the regions with opposite magnetization, the magnetic domains are usually topologically trivial in R space, preventing the realization of RK joint topological matter, like RK-SK.

In summary, we propose that the concept of the RK-SK state with external field–tunable N_{CBS} may appear when the SK state exists in a QAH insulator under certain conditions. Beyond the conventional SK states that can mainly be used by creation and annihilation, the number and chirality of CBS provide additional degrees of freedoms for quantum-state manipulations. Combining DFT calculations and MC simulations, we predict the ML $MnBi_2X_2Te_2$ is a unique platform to realize the multiple-space topology cross-over from K-space QAHE to R-space SK/SkX states. Most importantly, the external field–tunable RK-SK/SkX states can appear in a certain region of the ε–B_z diagram. Our findings not only may provide an idea to design SK states beyond the traditional ones, but also, they may provide opportunities to explore interplay and cross-over phenomena between multiple-space topologies and generate conceptual dissipationless spintronic applications.

Materials and Methods

DFT Calculations. The DFT calculations were performed using the Vienna ab initio Simulation Package (VASP) (62). In our calculations, the Perdew–Burke–Ernzerhof functional (63) was used to approximate the exchange correlation functional in the Kohn–Sham equation, and the projector-augmented wave method (64) was chosen to treat the core electrons. The energy cutoff for the plane-wave basis was chosen to be 400 eV, and the convergence criterion for the total energy was set to be 1.0×10^{-8} eV in all the calculations. A 20-Å vacuum layer was adopted to avoid the influence of the periodic images. An $18 \times 18 \times 1$ uniform Γ-centered k-point mesh was used to ensure the accuracy of our calculations. The rotationally invariant generalized gradient approximation (GGA) + U method (65) was used to correct the strong correlation effect derived from the partially occupied Mn-3d states. The value of effective Hubbard U_{eff} was chosen to be 3.0 eV, which was verified to be accurate and suitable to describe the electronic structures of $MnBi_2Te_4$ family materials (7, 40).

The phonon dispersion in the FM configuration was obtained using the finite displacement method. First, the crystal structure was relaxed until the force of each atom is less than 0.001 eV/Å. Second, the $5 \times 5 \times 1$ supercell combined with the $3 \times 3 \times 1$ uniform Γ-centered k-point mesh was used to perform self-consistent calculations to obtain the force constant matrix. Finally, the Fourier transform and diagonalization of the force constant matrix were performed using the Phonopy Package (66).

The thermodynamic stabilities of ML $MnBi_2X_2Te_2$ were confirmed by performing ab initio molecular dynamics simulations as implemented in VASP. We employed the NVT canonical ensemble and the Nosé–Hoover thermostat (67, 68) to preform simulations. The energy cutoff for the plane-wave basis was set to be 350 eV, and the convergence criterion for the total energy was set to be 1.0×10^{-6} eV. Here, the $5 \times 5 \times 1$ supercells combined with the single Γ-point were adopted to perform simulations, and the time step was set to be 2 fs. All simulations were performed for 8 ps (4,000 steps) to ensure that the systems reach equilibrium.

Tight-Binding Model and Edge-States Calculations. The tight-binding model was generated using the projected Wannier functions, which were constructed by projecting the DFT-calculated Blöch-wave functions into the Bi–*p*, Mn–*d*, *X*–*p*, and Te–*p* atomic orbitals. Based on the effective Hamiltonian matrix, the electronic band structure was fitted using the Wannier function interpolation approach as implemented in the Wannier90 Package (69). The edge state was calculated by iteratively solving the surface Green's function of the semiinfinite system (70).

Magnetic Interaction and MC Simulations. The magnetic interaction matrix was calculated using the four-states energy mapping method (71). Here, all matrix elements were obtained by performing the GGA + *U* calculations including the SOC effect and constraining the direction of magnetic moments. The $3 \times 3 \times 1$ supercell was used to remove the interactions caused by the periodic boundary conditions; meanwhile, the $4 \times 4 \times 1$ Γ-centered *k*-point mesh was adopted to maintain the same density of grid as in the unit cell calculations. The total energy was converged to $<1.0 \times 10^{-7}$ eV for each supercell to ensure the reliability of the calculated magnetic interaction parameters.

The *R*-space spin texture was obtained by performing the classical MC simulations, in which the metropolis algorithm was adopted to generate spin configurations according to the Boltzmann probability distribution (72). Starting from the random initial spin configuration at 50 K, we performed 4.0×10^5 MC steps at each temperature and slowly cooled down the temperature with 100 temperature steps to obtain the spin texture at near 0 K for each MC simulation work. The $100 \times 100 \times 1$ supercell with the periodic boundary conditions was adopted to perform simulations. Importantly, we emphasize that all the simulations were carefully performed several times with different initial spin configurations in order to confirm that our results were not influenced by the randomness of initial choices. We also performed MC simulations on the larger $120 \times 120 \times 1$ supercell to analysis the size effect, which generate the same results as the calculations using the $100 \times 100 \times 1$ supercell.

Supporting Information. *SI Appendix* includes detailed discussions about the crystal structures and the magnetic configurations, the analysis of the orbital projections for the band structures, the band structures under different external strains, the *R*-space spin textures under different external strains and magnetic fields, and other related results.

Data Availability. All study data are included in the article and/or *SI Appendix*.

ACKNOWLEDGMENTS. We thank Dr. Wujun Shi and Dr. Yizhou Liu for helpful discussions. Y.L., H.L., and B.H. acknowledge support from National Natural Science Foundation of China (NSFC) Grants 11634003 and 12088101 and NSAF Grant U1930402. S.X. and W.D. acknowledge support from Basic Science Center Project of NSFC Grant 51788104 and the Beijing Advanced Innovation Center for Future Chip. Parts of the calculations were performed at Tianhe2-JK at the Computational Science Research Center.

Author affiliations: [a]Beijing Computational Science Research Center, Beijing 100193, China; [b]State Key Laboratory of Low Dimensional Quantum Physics, Department of Physics, Tsinghua University, Beijing 100084, China; [c]School of Physics, Beihang University, Beijing 100191, China; [d]Department of Materials Science and Engineering, University of Washington, Seattle, WA 98195; [e]Department of Physics, Beijing Normal University, Beijing 100875, China; [f]Institute for Advanced Study, Tsinghua University, Beijing 100084, China; and [g]Frontier Science Center for Quantum Information, Beijing 100084, China

1. F. D. M. Haldane, Model for a quantum Hall effect without Landau levels: Condensed-matter realization of the "parity anomaly." *Phys. Rev. Lett.* **61**, 2015–2018 (1988).
2. H. Weng, R. Yu, X. Hu, X. Dai, Z. Fang, Quantum anomalous Hall effect and related topological electronic states. *Adv. Phys.* **64**, 227–282 (2015).
3. C. X. Liu, S. C. Zhang, X. L. Qi, The quantum anomalous Hall effect: Theory and experiment. *Annu. Rev. Condens. Matter Phys.* **7**, 301–321 (2016).
4. R. Yu *et al.*, Quantized anomalous Hall effect in magnetic topological insulators. *Science* **329**, 61–64 (2010).
5. C. Z. Chang *et al.*, Experimental observation of the quantum anomalous Hall effect in a magnetic topological insulator. *Science* **340**, 167–170 (2013).
6. J. Li *et al.*, Intrinsic magnetic topological insulators in van der Waals layered $MnBi_2Te_4$-family materials. *Sci. Adv.* **5**, eaaw5685 (2019).
7. D. Zhang *et al.*, Topological axion states in the magnetic insulator $MnBi_2Te_4$with the quantized magnetoelectric effect. *Phys. Rev. Lett.* **122**, 206401 (2019).
8. M. M. Otrokov *et al.*, Unique thickness-dependent properties of the van der Waals tnterlayer antiferromagnet $MnBi_2Te_4$films. *Phys. Rev. Lett.* **122**, 107202 (2019).
9. Y. Gong *et al.*, Experimental realization of an intrinsic magnetic topological insulator. *Chin. Phys. Lett.* **36**, 076801 (2019).
10. M. M. Otrokov *et al.*, Prediction and observation of an antiferromagnetic topological insulator. *Nature* **576**, 416–422 (2019).
11. Y. Deng *et al.*, Quantum anomalous Hall effect in intrinsic magnetic topological insulator $MnBi_2Te_4$. *Science* **367**, 895–900 (2020).
12. N. Nagaosa, Y. Tokura, Topological properties and dynamics of magnetic skyrmions. *Nat. Nanotechnol.* **8**, 899–911 (2013).
13. R. Wiesendanger, Nanoscale magnetic skyrmions in metallic films and multilayers: A new twist for spintronics. *Nat. Rev. Mater.* **1**, 16044 (2016).
14. A. Fert, N. Reyren, V. Cros, Magnetic skyrmions: Advances in physics and potential applications. *Nat. Rev. Mater.* **2**, 17031 (2017).
15. X. Zhang *et al.*, Skyrmion-electronics: Writing, deleting, reading and processing magnetic skyrmions toward spintronic applications. *J. Phys. Condens. Matter* **32**, 143001 (2020).
16. Y. Tokura, N. Kanazawa, Magnetic skyrmion materials. *Chem. Rev.* **121**, 2857–2897 (2021).
17. Y. Tokura, M. Kawasaki, N. Nagaosa, Emergent functions of quantum materials. *Nat. Phys.* **13**, 1056–1068 (2017).
18. A. Neubauer *et al.*, Topological Hall effect in the *A* phase of MnSi. *Phys. Rev. Lett.* **102**, 186602 (2009).
19. J. Matsuno *et al.*, Interface-driven topological Hall effect in $SrRuO_3$-$SrIrO_3$bilayer. *Sci. Adv.* **2**, e1600304 (2016).
20. C. Liu *et al.*, Dimensional crossover-induced topological Hall effect in a magnetic topological insulator. *Phys. Rev. Lett.* **119**, 176809 (2017).
21. S. Mühlbauer *et al.*, Skyrmion lattice in a chiral magnet. *Science* **323**, 915–919 (2009).
22. X. Z. Yu *et al.*, Near room-temperature formation of a skyrmion crystal in thin-films of the helimagnet FeGe. *Nat. Mater.* **10**, 106–109 (2011).
23. S. Seki, X. Z. Yu, S. Ishiwata, Y. Tokura, Observation of skyrmions in a multiferroic material. *Science* **336**, 198–201 (2012).
24. S. Heinze *et al.*, Spontaneous atomic-scale magnetic skyrmion lattice in two dimensions. *Nat. Phys.* **7**, 713–718 (2011).
25. N. Romming *et al.*, Writing and deleting single magnetic skyrmions. *Science* **341**, 636–639 (2013).
26. C. Moreau-Luchaire *et al.*, Additive interfacial chiral interaction in multilayers for stabilization of small individual skyrmions at room temperature. *Nat. Nanotechnol.* **11**, 444–448 (2016).
27. Q. Tong, F. Liu, J. Xiao, W. Yao, Skyrmions in the moiré of van der Waals 2D magnets. *Nano Lett.* **18**, 7194–7199 (2018).
28. M. Akram *et al.*, Moiré skyrmions and chiral magnetic phases in twisted CrX_3 (X = I, Br, and Cl) bilayers. *Nano Lett.* **21**, 6633–6639 (2021).
29. Y. Wu *et al.*, Néel-type skyrmion in WTe_2/Fe_3GeTe_2van der Waals heterostructure. *Nat. Commun.* **11**, 3860 (2020).
30. I. Dzyaloshinskii, A thermodynamic theory of "weak" ferromagnetism of antiferromagnetics. *J. Phys. Chem. Solids* **4**, 241–255 (1958).
31. T. Moriya, Anisotropic superexchange interaction and weak ferromagnetism. *Phys. Rev.* **120**, 91–98 (1960).
32. K. Hamamoto, M. Ezawa, N. Nagaosa, Quantized topological Hall effect in skyrmion crystal. *Phys. Rev. B Condens. Matter Mater. Phys.* **92**, 115417 (2015).
33. J. L. Lado, J. Fernández-Rossier, Quantum anomalous Hall effect in graphene coupled to skyrmions. *Phys. Rev. B Condens. Matter Mater. Phys.* **92**, 115433 (2015).
34. J. Jiang *et al.*, Concurrence of quantum anomalous Hall and topological Hall effects in magnetic topological insulator sandwich heterostructures. *Nat. Mater.* **19**, 732–737 (2020).
35. R. Xiao *et al.*, Mapping the phase diagram of the quantum anomalous Hall and topological Hall effects in a dual-gated magnetic topological insulator heterostructure. *Phys. Rev. Res.* **3**, L032004 (2021).
36. A. Y. Lu *et al.*, Janus monolayers of transition metal dichalcogenides. *Nat. Nanotechnol.* **12**, 744–749 (2017).
37. J. Zhang *et al.*, Janus monolayer transition-metal dichalcogenides. *ACS Nano* **11**, 8192–8198 (2017).
38. L. Zhang *et al.*, Janus graphene from asymmetric two-dimensional chemistry. *Nat. Commun.* **4**, 1443 (2013).
39. C. Zhang, Y. Nie, S. Sanvito, A. Du, First-principles prediction of a room-temperature ferromagnetic Janus VSSe monolayer with piezoelectricity, ferroelasticity, and large valley polarization. *Nano Lett.* **19**, 1366–1370 (2019).
40. Y. Li, Z. Jiang, J. Li, S. Xu, W. Duan, Magnetic anisotropy of the two-dimensional ferromagnetic insulator $MnBi_2Te_4$. *Phys. Rev. B* **100**, 134438 (2019).
41. J. Y. You, X. J. Dong, B. Gu, G. Su, Electric field induced topological phase transition and large enhancements of spin-orbit coupling and Curie temperature in two-dimensional ferromagnetic semiconductors. *Phys. Rev. B* **103**, 104403 (2021).
42. H. Xiang, C. Lee, H. J. Koo, X. Gong, M. H. Whangbo, Magnetic properties and energy-mapping analysis. *Dalton Trans.* **42**, 823–853 (2013).
43. D. Soriano, M. I. Katsnelson, J. Fernández-Rossier, Magnetic two-dimensional chromium trihalides: A theoretical perspective. *Nano Lett.* **20**, 6225–6234 (2020).

44. J. B. Goodenough, Theory of the role of covalence in the perovskite-type manganites [La, *M*(II)]MnO_3. *Phys. Rev.* **100**, 564–573 (1955).
45. J. Kanamori, Superexchange interaction and symmetry properties of electron orbitals. *J. Phys. Chem. Solids* **10**, 87–98 (1959).
46. C. Xu *et al.*, Topological spin texture in Janus monolayers of the chromium trihalides $Cr(I, X)_3$. *Phys. Rev. B* **101**, 060404 (2020).
47. Y. Zhang *et al.*, Emergence of skyrmionium in a two-dimensional $CrGe(Se, Te)_3$ Janus monolayer. *Phys. Rev. B* **102**, 241107 (2020).
48. Z. Shen *et al.*, Strain tunable skyrmions and strong Dzyaloshinskii-Moriya interaction in two-dimensional Janus $Cr(X, Y)_3$ trihalides monolayers. arXiv [Preprint] (2021). https://arxiv.org/abs/2109.00723 (Accessed 2 September 2021).
49. J. Yuan *et al.*, Intrinsic skyrmions in monolayer Janus magnets. *Phys. Rev. B* **101**, 094420 (2020).
50. J. Liang *et al.*, Very large Dzyaloshinskii-Moriya interaction in two-dimensional Janus manganese dichalcogenides and its application to realize skyrmion states. *Phys. Rev. B* **101**, 184401 (2020).
51. Q. Cui, J. Liang, Z. Shao, P. Cui, H. Yang, Strain-tunable ferromagnetism and chiral spin textures in two-dimensional Janus chromium dichalcogenides. *Phys. Rev. B* **102**, 094425 (2020).
52. J. Z. Fang *et al.*, Intermediate anomalous Hall states induced by noncollinear spin structure in the magnetic topological insulator $MnBi_2Te_4$. *Phys. Rev. B* **104**, 054409 (2021).
53. S. Banerjee, J. Rowland, O. Erten, M. Randeria, Enhanced stability of skyrmions in two-dimensional chiral magnets with rashba spin-orbit coupling. *Phys. Rev. X* **4**, 031045 (2014).
54. A. Soumyanarayanan *et al.*, Tunable room-temperature magnetic skyrmions in Ir/Fe/Co/Pt multilayers. *Nat. Mater.* **16**, 898–904 (2017).
55. A. Siemens, Y. Zhang, J. Hagemeister, E. Y. Vedmedenko, R. Wiesendanger, Minimal radius of magnetic skyrmions: Statics and dynamics. *New J. Phys.* **18**, 045021 (2016).
56. M. Z. Hasan, C. L. Kane, Colloquium: Topological insulators. *Rev. Mod. Phys.* **82**, 3045–3067 (2010).
57. K. Motida, S. Miyahara, On the 90° exchange interaction between cations (Cr^{3+}, Mn^{2+}, Fe^{3+} and Ni^{2+}) in oxides. *J. Phys. Soc. Jpn.* **28**, 1188–1196 (1970).
58. K. Yosida, *Theory of Magnetism* (Springer-Verlag, Berlin, Germany, 1996), vol. 122.
59. Y. Li *et al.*, Electrically tunable valleytronics in quantum anomalous Hall insulating transition metal trihalides. *Phys. Rev. B* **98**, 201407 (2018).
60. D. Xiao, M. C. Chang, Q. Niu, Berry phase effects on electronic properties. *Rev. Mod. Phys.* **82**, 1959–2007 (2010).
61. C. X. Trang *et al.*, Crossover from 2D ferromagnetic insulator to wide band gap quantum anomalous Hall insulator in ultrathin $MnBi_2Te_4$. *ACS Nano* **15**, 13444–13452 (2021).
62. G. Kresse, J. Furthmüller, Efficient iterative schemes for *ab initio* total-energy calculations using a plane-wave basis set. *Phys. Rev. B Condens. Matter* **54**, 11169–11186 (1996).
63. J. P. Perdew, K. Burke, M. Ernzerhof, Generalized gradient approximation made simple. *Phys. Rev. Lett.* **77**, 3865–3868 (1996).
64. P. E. Blöchl, Projector augmented-wave method. *Phys. Rev. B Condens. Matter* **50**, 17953–17979 (1994).
65. S. L. Dudarev, G. A. Botton, S. Y. Savrasov, C. J. Humphreys, A. P. Sutton, Electron-energy-loss spectra and the structural stability of nickel oxide: An LSDA+U study. *Phys. Rev. B Condens. Matter Mater. Phys.* **57**, 1505–1509 (1998).
66. A. Togo, I. Tanaka, First principles phonon calculations in materials science. *Scr. Mater.* **108**, 1–5 (2015).
67. S. Nosé, A unified formulation of the constant temperature molecular dynamics methods. *J. Chem. Phys.* **81**, 511–519 (1984).
68. W. G. Hoover, Canonical dynamics: Equilibrium phase-space distributions. *Phys. Rev. A Gen. Phys.* **31**, 1695–1697 (1985).
69. G. Pizzi *et al.*, Wannier90 as a community code: New features and applications. *J. Phys. Condens. Matter* **32**, 165902 (2020).
70. M. P. L. Sancho, J. M. L. Sancho, J. M. L. Sancho, J. Rubio, Highly convergent schemes for the calculation of bulk and surface Green functions. *J. Phys. F Met. Phys.* **15**, 851–858 (1985).
71. H. J. Xiang, E. J. Kan, S. H. Wei, M. H. Whangbo, X. G. Gong, Predicting the spin-lattice order of frustrated systems from first principles. *Phys. Rev. B Condens. Matter Mater. Phys.* **84**, 224429 (2011).
72. N. Metropolis, A. W. Rosenbluth, M. N. Rosenbluth, A. H. Teller, E. Teller, Equation of state calculations by fast computing machines. *J. Chem. Phys.* **21**, 1087–1092 (1953).